Available online at www.sciencedirect.com
ScienceDirect
International Journal of Thermal Sciences 47 (2008) 1496–1503
International Journal of Thermal Sciences
www.elsevier.com/locate/ijts

A cavity-receiver containing a tubular absorber for high-temperature thermochemical processing using concentrated solar energy

Tom Melchior [a], Christopher Perkins [b], Alan W. Weimer [b], Aldo Steinfeld [a,c,*]

[a] *Department of Mechanical and Process Engineering, ETH Zurich, 8092 Zurich, Switzerland*
[b] *Department of Chemical and Biological Engineering, Engineering Center, University of Colorado at Boulder, CO 80309-0424, USA*
[c] *Solar Technology Laboratory, Paul Scherrer Institute, 5232 Villigen, Switzerland*

Received 26 August 2007; received in revised form 8 December 2007; accepted 13 December 2007

Available online 16 January 2008

Abstract

A solar chemical reactor consisting of a cylindrical cavity-receiver containing a tubular ceramic absorber is considered for performing thermochemical processes using concentrated solar radiation as the energy source of high-temperature process heat. The model chemical reaction selected is the thermal dissociation of ZnO into its elements, which proceeds endothermically at above 1800 K and is part of a 2-step H_2O-splitting thermochemical cycle for H_2 production. A lab-scale 5 kW reactor prototype is fabricated and subjected to high-flux solar irradiation in the range 448–2125 kW/m^2. A heat transfer reactor model is formulated that encompasses the governing mass and energy conservation equations coupling radiation/convection/conduction heat transfer to the chemical kinetics, and their solution by Monte Carlo ray-tracing and finite difference techniques. Validation was accomplished by comparing numerically computed and experimentally measured temperatures and reaction rates in the 1780–1975 K range. The reactor model is further applied to simulate a continuous thermochemical process, identify major sources of irreversibility, and predict solar-to-chemical energy conversion efficiencies.

Keywords: Solar; Energy; Cavity; Reactor; Receiver; Thermochemical cycle; Water splitting; Hydrogen; Zinc; Heat transfer

1. Introduction

Solar thermochemical processes make use of concentrated solar energy as the source of process heat for driving high-temperature endothermic reactions and, consequently, storing solar energy in the form of transportable chemical fuels [1]. Solar reactors for highly concentrated solar applications usually feature the use of a cavity-type configuration, i.e. a well insulated enclosure designed to effectively capture incident solar radiation entering through a small opening—the *aperture*. The larger the ratio of cavity area to the aperture area, the closer the cavity-receiver approaches a blackbody absorber, but at the expense of higher conduction losses through the insulated cavity walls. Smaller apertures will also reduce re-radiation losses but they intercept less sunlight. Consequently, the optimum aperture size becomes a compromise between maximizing radiation capture and minimizing radiation losses [2]. To some extent, the aperture size may be reduced with the help of non-imaging secondary concentrators, e.g., compound parabolic concentrators (CPC), placed at the receiver's aperture in tandem with the primary concentrating system [3]. The solar cavity-receiver considered contains an absorber that is exposed to concentrated solar radiation entering through the cavity's aperture and to IR radiation emitted by the hot cavity walls. An absorber with opaque walls transfers the absorbed heat to the chemical reaction site by conduction through its walls. The limitations imposed by the materials of construction of the absorber are the maximum operating temperature, inertness to the chemical reaction, thermal conductivity, radiative absorptance, and resistance to thermal shocks.

The thermal dissociation of ZnO(s) into its elements has been selected as the model thermochemical process. This reaction, which is part of a 2-step H_2O-splitting thermochemical cycle for H_2 production, proceeds endothermically ($\Delta H^\circ_{298\,K} = 350$ kJ/mol) at above 1800 K [4–6]. Corresponding activa-

* Corresponding author.
E-mail address: aldo.steinfeld@eth.ch (A. Steinfeld).

1290-0729/$ – see front matter
doi:10.1016/j.ijthermalsci.2007.12.003

Nomenclature

A_i	surface area per unit length of control volume i ... ($m^2\,m^{-1}$)
A_{ZnO}	reactant surface area per unit length ... ($m^2\,m^{-1}$)
a	conductance coefficient ... ($W\,m^{-1}\,K^{-1}$)
d	diameter ... (m)
$e_{\lambda b}$	Planck's blackbody emissive power ($W\,m^{-2}\mu m^{-1}$)
$F_{0-\lambda T}$	blackbody fractional function, $F_{0-\lambda T} = \int_0^{\lambda} e_{\lambda b}(T)\,d\lambda/\sigma T^4$
$F^{-1}_{0-\lambda T}$	inverse fractional function
h	convective heat transfer coefficient ... ($W\,m^{-2}\,K^{-1}$)
k	thermal conductivity ... ($W\,m^{-1}\,K^{-1}$)
l	reaction zone length ... (m)
m	number of grid points in radial direction
$\dot{m}$	decomposition rate ... ($g\,m^{-2}\,s^{-1}$)
n	number of grid points in angular direction
$\dot{n}_{0,ZnO}$	incoming molar flow rate of ZnO ... ($mol\,s^{-1}$)
$\dot{n}_x$	molar flow rate of species x ... ($mol\,s^{-1}$)
N_{ray}	sample of rays
Nu	Nusselt number
q	heat flux ... ($W\,m^{-2}$)
Q	power per unit length ... ($W\,m^{-1}$)
r	polar coordinate; radius ... (m)
$\Re_\lambda$	random number from a uniform set [0, 1]
Ra_δ	Rayleigh number
T	temperature ... (K)
X_{ZnO}	reaction extent
w_{ap}	aperture width ... (m)

Greek symbols

δ	annular gap size ... (m)
ΔH	enthalpy change ... ($kJ\,mol^{-1}$)
$\Delta H^{\circ}_{298\,K}$	Standard enthalpy of formation at 298 K ... ($kJ\,mol^{-1}$)
Δr	radial mesh size ... (m)
ΔV	volume of unit thickness ... (m^2)
$\Delta\varphi$	angular mesh size ... (rad)
δ_{ij}	Kronecker function ($\delta_{ij} = 1$ for $i = j$; $\delta_{ij} = 0$ for $i \neq j$)
ε	emissivity
η	energy conversion efficiency
θ	CPC acceptance angle ... (rad)
λ	wavelength ... (m)
λ_c	cut-off wavelength ... (m)
ρ	CPC reflectivity
σ	Stefan–Boltzmann constant ... ($5.67 \times 10^{-8}\,W\,m^{-2}\,K^{-4}$)
ϕ	polar coordinate ... (rad)

Subscripts

a	absorber
c	cavity
center	absorber center
i	angular index of a grid point
in	inner side of absorber/cavity
j	radial index of a grid point
out	outer side of absorber/cavity
p	grid point
s	surface
λ	spectral
0	surroundings
3 mm	3 mm behind the inner cavity surface

Superscripts

f	iteration step

tion energies are in the range of 310–350 kJ/mol [6]. Previous solar reactor designs featured the direct irradiation of ZnO through transparent quartz windows [7–10], providing efficient heat transfer directly to the reaction site. However, the window becomes a critical and troublesome component under high-pressure, severe gas environments, and scale-up designs. The use of a protecting partition plate introduced between the window and the reaction chamber has been suggested to bypass this problem [11]. The alternative design examined in this paper features a cavity-receiver containing an opaque absorber that serves as the reaction chamber. This arrangement eliminates the need for a window at the expense of having a less efficient heat transfer—by conduction—through the ceramic walls of the absorber. This paper describes the design and fabrication of a 5 kW reactor prototype based on such a configuration, and presents its thermal performance when subjected to concentrated solar energy. A radiative heat transfer model previously formulated for this reactor configuration [12] is extended to include coupling with conduction/convection heat transfer and to the chemical kinetics, and validated by comparing numerically calculated and experimentally measured temperature distributions. The validation is accomplished for a continuous flow of Ar and for a batch chemical process to examine the capability of this receiver-reactor concept to transfer solar process heat to a working fluid flow and to solid reactants at ultra high temperatures. Practical problems associated with construction materials exposed to high-flux irradiation and temperatures exceeding 1900 K are discussed.

2. Solar reactor configuration

The solar reactor configuration is shown schematically in Fig. 1. The radiation source is ETH's High-Flux Solar Simulator (HFSS) [13]: a high-pressure Argon arc enclosed in a 27 mm-diameter 200 mm-length water-cooled quartz envelope and closed-coupled to a precision optical reflector to produce an intense beam of concentrated thermal radiation, mostly in the visible and IR spectrum, that approaches the heat transfer characteristics of highly concentrating solar systems. The focusing mirror is an horizontal-axis trough of elliptical cross section and

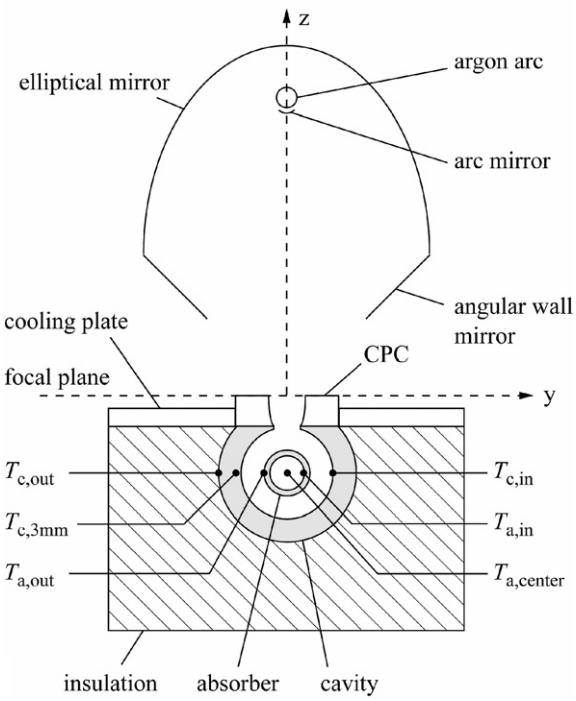

Fig. 1. Solar reactor configuration: ETH's High-Flux Solar Simulator delivers concentrated thermal radiation to the cylindrical cavity-receiver containing the tubular absorber that serves as the reaction chamber. A CPC is incorporated to the cavity's aperture, with its entrance at the focal plane of the solar concentrating system, and its exit matching the aperture of the cavity (dimensions not to scale).

is positioned with one of its linear foci coinciding with the arc. The focal plane of the solar simulator is thus defined as the horizontal plane perpendicular to the ellipse's major axis containing the second linear focus. With this arrangement, radiative power fluxes exceeding 4500 kW/m^2 are attained at the focal plane and confined within a 45° rim angle. Power, power fluxes, and temperatures can be adjusted by simply varying the electrical input power to the arc electrodes.

The solar cavity-receiver consists of a cylinder made of 10 wt% YO_2-stabilized ZrO_2, with an inner radius $r_{c,in} = 2.54$ cm and an outer radius $r_{c,out} = 3.81$ cm, and lined with Al_2O_3 insulation. It has a windowless slab (rectangular) aperture of width 1.414 cm and length 15 cm. The Al_2O_3 tubular absorber, with an inner radius $r_{a,in} = 0.9525$ cm and an outer radius $r_{a,out} = 1.27$ cm, is positioned concentric with the cylindrical cavity. A water-cooled trough CPC is incorporated to the cavity's aperture, with its 150 × 20 mm rectangular entrance at the focal plane of the solar concentrating system, and its exit matching the aperture. The result of such an optical arrangement is an augmentation of the mean radiation flux over the aperture by a factor of $\rho/\sin\theta$, where ρ is the CPC's reflectivity and θ its acceptance angle—in this case equal to the rim angle of the solar concentrating system, 45°. A water-cooled copper plate mounted on top of the reactor serves as protective shield for spilled radiation. Temperatures are measured with type-B and type-K thermocouples at four locations indicated in Fig. 1: at the outer surface of the absorber ($T_{a,out}$), at 3 mm behind the inner cavity surface ($T_{c,3\,mm}$), at the center of the absorber ($T_{a,center}$), and at the outer cavity surface ($T_{c,out}$).

3. Heat transfer analysis

The model domain, consisting of the cavity and absorber, is divided into a large number of control volumes having opaque, isothermal, non-gray, and diffuse surfaces. Two-dimensional steady-state mass and energy conservation equations are formulated for each control volume and solved by Monte Carlo (MC) ray-tracing and finite-difference techniques.

Monte Carlo. The radiative exchange inside the cavity is solved by applying the 3D pathlength-based MC ray-tracing method [14]. The methodology consists of following stochastic paths of a large number of rays as they travel through the interacting boundary surfaces. Each ray, which has an associated direction and wavelength determined from the appropriate probability density functions, undergoes absorption or reflection at the absorber and/or cavity surfaces. The medium is assumed non-participating. Sources of stochastic rays are incoming solar radiation through the aperture and IR radiation emitted by the inner cavity surface and outer absorber surface. The concentrated solar radiation exiting the CPC and entering the cavity is assumed to have a uniform directional distribution over half hemisphere and a uniform power flux distribution over the aperture. Planck's spectral distribution for a 5780 K blackbody is used to simulate the solar spectrum. The wavelength assigned to a generic ray is found from the inverse fractional function:

$$\lambda = F^{-1}_{0-\lambda T}(\Re_\lambda)/T \tag{1}$$

for $T = 5780$ K, where $\Re_\lambda$ denotes a random number chosen from a uniform set [0, 1]. The wavelength of emission from a surface is found by solving the implicit equation

$$\Re_\lambda = \frac{\int_0^\lambda \varepsilon_\lambda e_{\lambda b}(\lambda, T)\,\mathrm{d}\lambda}{\varepsilon\sigma T^4} \tag{2}$$

where the Planck's blackbody spectral emissive power $e_{\lambda b}(\lambda, T)$ is evaluated at the temperature of the location of emission. Eq. (2) is solved by applying the 2-band gray approximation using values of hemispherical spectral emissivity $\varepsilon_{\lambda,1}$ and $\varepsilon_{\lambda,2}$ given in Table 1, yielding:

$$\lambda = \begin{cases} \dfrac{F^{-1}_{0-\lambda T}(\frac{\varepsilon}{\varepsilon_{\lambda,1}}\Re_\lambda)}{T} \\ \quad \text{for } \Re_\lambda \leqslant \varepsilon_{\lambda,1} F_{0-\lambda_c T}/\varepsilon \\ \dfrac{F^{-1}_{0-\lambda T}[F_{0-\lambda_c T} + \frac{\varepsilon}{\varepsilon_{\lambda,2}}(\Re_\lambda - \frac{\varepsilon_{\lambda,1}}{\varepsilon}F_{0-\lambda_c T})]}{T} \\ \quad \text{for } \Re_\lambda > \varepsilon_{\lambda,1} F_{0-\lambda_c T}/\varepsilon \end{cases} \tag{3}$$

with the total emissivity ε calculated at the surface temperature T,

$$\varepsilon(T) = \varepsilon_{\lambda,1} F_{0-\lambda_c T} + \varepsilon_{\lambda,2}(1 - F_{0-\lambda_c T}) \tag{4}$$

The history of a generic ray is a complete random sequence that terminates when it is absorbed or lost through the aperture to the surroundings. Statistically meaningful results are obtained for sample of rays N_{ray} of 10^5.

Table 1
Two-band approximation of spectral emissivity of alumina and zirconia

	Al_2O_3 (absorber)	ZrO_2 (cavity)
Emissivity $\varepsilon_{\lambda,1}$	0.4	0.2
Emissivity $\varepsilon_{\lambda,2}$	0.95	0.9
Cut-off wavelength λ_c [m]	5×10^{-6}	6×10^{-6}

Values taken from Ref. [15].

Energy conservation. Steady-state energy balance for the system yields:

$$\sum Q = 0 = Q_{\text{solar}} - Q_{\text{reradiation}} - Q_{\text{conduction}} - Q_{\text{convection}} - Q_{\text{gas}} - Q_{\text{reactants}} - Q_{\text{chemistry}} \quad (5)$$

where Q_{solar} is the solar power input to the cavity, $Q_{\text{reradiation}}$ is the power lost by re-radiation through the aperture, $Q_{\text{conduction}}$ is the total power lost by conduction through the reactor walls, $Q_{\text{convection}}$ is the power lost by natural convection to the surroundings, Q_{gas} is the power transferred by convection to the Ar gas stream inside the absorber, $Q_{\text{reactants}}$ is power used for heating the reactants, and $Q_{\text{chemistry}}$ is the power used for driving the chemical reaction. Their values are given in power per unit length of the tubular absorber (W/m) for the 2D-simulations. The steady-state energy conservation equation applied to each sub-system, i.e. the cavity and the absorber, is given by:

$$-\frac{\partial}{\partial r}\left(rk\frac{\partial T}{\partial r}\right) - \frac{\partial}{\partial \varphi}\left(\frac{k}{r}\frac{\partial T}{\partial \varphi}\right) = q \quad (6)$$

The discretized subsystems consist of n nodes in angular direction and m nodes in radial direction, with n and m being set to 20 and 10 for the absorber, and 40 and 20 for the cavity. The boundary conditions are:

at the outer absorber and inner cavity surface,

$$q|_s = q_{\text{emission}} - q_{\text{absorption}} + q_{\text{convection}} \quad (7)$$

at the inner absorber surface,

$$q|_s = q_{\text{gas}} + q_{\text{reactants}} + q_{\text{chemistry}} \quad (8)$$

at the outer cavity surface,

$$q|_s = q_{\text{conduction}} \quad (9)$$

which, when discretized and solved for the node temperature $T_{i,j}$ yields:

$$T_{i,j} = \frac{1}{a_p}(a_{i,j\pm1}T_{i,j\pm1} + a_{i-1,j}T_{i-1,j} + a_{i+1,j}T_{i+1,j} - A_i q|_s) \quad (10)$$

with the coefficients given by:

$$\text{in the radial direction:} \quad a_{i,j\pm1} = \frac{k_{i,j\pm1/2}r_{i,j\pm1/2}\Delta\varphi}{\Delta r} \quad (11)$$

$$\text{in the angular direction:} \quad a_{i\pm1,j} = \frac{k_{i\pm1/2,j}\Delta r}{r_{i\pm1/2,j}\Delta\varphi} \quad (12)$$

and the center-point coefficient a_p being the sum of all neighbor coefficients. The temperature-dependent values of k_{Al2O3} and k_{ZrO2} are taken from Refs. [16] and [17], respectively. For nodes located at the water-cooled copper plate boundary, $T_{i,j}|_{\text{Cu Plate}} = T_0$. The radiative flux emitted by surface A_i at $T_{i,1}$ is $q_{\text{emission},i} = \varepsilon_i \sigma T_{i,1}^4$. $q_{\text{absorption},i}$ is found by MC.

Natural convection has been considered in previous studies for horizontal concentric and eccentric annuli [18–22], for large cubical cavities [23], for single tube cylindrical frustum shaped receivers [24], for spherical, hemispherical, and cylindrical cavity-receivers [25–27]. However, none of these investigations is applicable in the present geometric configuration that contains a hot body inside the cavity and an upward-facing aperture. Transient 3D natural convective heat transfer was computed using CFD software package ANSYS CFX 10.0 [28]. Steady-state heat transfer was attained after 1s, yielding the following correlations of the Nusselt number at the absorber Nu_δ (based on the annulus gap size $\delta = r_{c,in} - r_{a,out}$) and at aperture $Nu_{w_{ap}}$ (based on the aperture width w_{ap}):

$$Nu_\delta = h \cdot \delta / k_{\text{air}} = 0.1331 \cdot Ra_\delta^{0.3107}\left(\frac{T_{a,out} - T_{c,in}}{T_0}\right)^{0.3411} \quad (13)$$

$$Nu_{w_{ap}} = h \cdot w_{ap} / k_{\text{air}} = 0.7515 \cdot Ra_\delta^{0.3334} \cdot \left(\frac{T_{a,out} - T_{c,in}}{T_0}\right)^{-0.1386} \quad (14)$$

which are valid for $50 < Ra_\delta < 1400$ and $0.65 < (T_{a,out} - T_{c,in})/T_0 < 4.00$. Fig. 2 shows the parity plots of the Nusselt number, the correlation coefficient, and the standard deviation of the fit. Properties of air are evaluated at the volume-mean temperature [19]:

$$T_{\text{mean,air}} = T_{a,out} - (T_{a,out} - T_{c,in})\left\{\frac{1}{1 - (r_{a,out}/r_{c,in})^2} + \frac{1}{2\ln(r_{a,out}/r_{c,in})}\right\} \quad (15)$$

The Nusselt number for internal flow in a circular tube $Nu_{d_{a,in}} = hd_{a,in}/k_{Ar}$, needed for the calculation of q_{gas}, is 4.36 [22]. The temperature-dependent thermal conductivity of Ar, k_{Ar}, is taken from Ref. [29]. $q_{\text{conduction}}$ is calculated using 1D radial steady-state conduction heat transfer through the insulation. The reactant ZnO(s) enters the reactor at $T_0 = 300$K and is heated to the reactor temperature at $T_{a,in}$. Thus,

$$q_{\text{reactants}} = \frac{\dot{n}_{0,\text{ZnO}}\Delta H|_{\text{ZnO at } T_0 \to \text{ZnO at } T_{a,in}}}{2\pi r_{a,in} l} \quad (16)$$

The reaction extent $X_{\text{ZnO}} = 1 - \frac{\dot{n}_{\text{ZnO}}}{\dot{n}_{0,\text{ZnO}}}$ is determined at the reactor temperature based on the Arrhenius-type decomposition rate law [30],

$$\dot{m} = 1.356 \times 10^9 \mathrm{e}^{-\left(\frac{328{,}500}{8.314T}\right)} \mathrm{g\,m^{-2}\,s^{-1}} \quad (17)$$

assuming a reaction zone length $l = 15$ cm, an initial particle diameter of 7×10^{-6} m, and an Ar carrier mass flow rate of 1 l_n/min[1]. For simplicity, the gas velocity and residence time

[1] l_n means litres under standard conditions at 273.15 K and 1 atm.

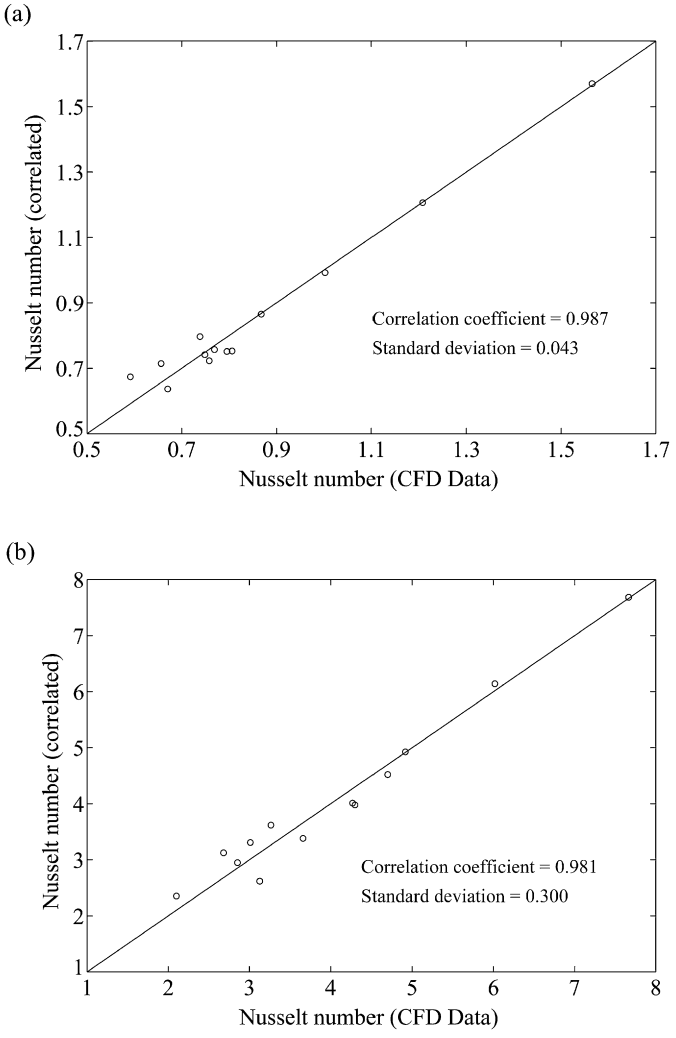

Fig. 2. Parity plots of Nusselt number for natural convective heat transfer: (a) at the absorber; (b) at the aperture.

was evaluated for a plug flow at $T_{a,in}$. The power absorbed by the chemical reaction is then:

$$q_{\text{chemistry}} = \frac{\dot{n}_{\text{Zn}} \Delta H|_{\text{ZnO at } T_{a,in} \rightarrow \text{Zn(g)}+0.5\text{O}_2 \text{ at } T_{a,in}}}{2\pi r_{a,in} l} \tag{18}$$

where $\dot{n}_{\text{Zn}} = X_{\text{ZnO}} \dot{n}_{0,\text{ZnO}}$ is the molar flow rate of ZnO decomposed. Note that heat transfer to the chemical reactants and gas flow occurs via a combined radiation/conduction/convection mode, but its detailed analysis is not required. The model may be also extended to account for particle dynamics in a two-phase flow. The system of equations is solved iteratively with the Gauss–Seidel method using the convergence criterion $|1 - T_{i,j}^{f-1}/T_{i,j}^{f}| \leqslant 10^{-3}$ for every single node. The superscript f denotes the iteration step.

4. Numerical results and experimental validation

Radiative power flux. The incoming radiative flux distribution at the focal plane was measured optically on a Al_2O_3-plasma-coated Lambertian target with a CCD camera equipped with optical filters and calibrated with a Kendall radiometer (error of ±8%). Fig. 3 shows the measured radiative flux distribution

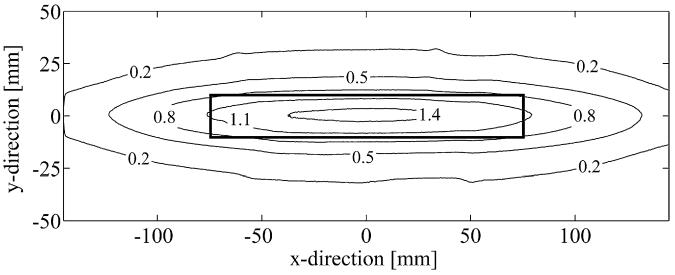

Fig. 3. Solar radiative flux distribution (in MW/m^2) measured at the focal plane of ETH's High-Flux Solar Simulator. The rectangle with dimensions 150 × 20 mm represents the entrance of the CPC.

Table 2
Measured HFSS's arc current, peak incident radiative flux at the focal plane, mean incident radiative flux at CPC entrance, and incoming power into the cavity per unit length of absorber

Arc current [A]	Peak flux [kW/m^2]	Mean flux at CPC [kW/m^2]	Q_{solar} [kW/m]
100	448	335	5.4
200	930	745	11.9
300	1490	1215	19.4
400	2125	1769	28.3

at the CPC entrance for an arc current of 300 A. The peak flux was 1490 kW/m^2 and the mean over the CPC entrance was 1215 kW/m^2. A mean flux of 1719 kW/m^2 can be achieved at the CPC exit that matches the aperture provided $\rho = 1$. Integration of the power flux over the CPC entrance (150 × 20 mm) yielded a total solar power input of 3.65 kW. Table 2 gives the measured peak radiative flux at the focal plane, mean radiative flux over the CPC entrance, and the input solar power into the cavity Q_{solar} per unit length of absorber, for arc currents of 100, 200, 300 and 400 A.

Validation of the reactor model in terms of measured temperatures was performed for continuous-mode experiments using an Ar flow but without chemical reaction ($q_{\text{chemistry}} = 0$). Validation of the kinetic rate law (Eq. (17)) in terms of the measured reaction rates was performed for batch-mode experiments using a pre-fed batch of ZnO.

A set of 7 representative runs using an Ar mass flow rate of 1 l_n/min and without chemical reaction were carried out for the continuous-mode experimental validation of the model. Fig. 4 shows the numerically calculated (curves) and experimentally measured (markers) temperatures at the inner absorber surface $T_{a,in}$, the inner cavity surface $T_{c,in}$, the outer cavity surface $T_{c,out}$, and 3 mm behind the inner cavity surface $T_{c,3\text{ mm}}$, as a function of the incoming solar power per until length Q_{solar} in the range from 5.4 to 28.3 kW/m. Not shown are the calculated and measured temperatures on the outer absorber surface as they practically coincide with the inner absorber temperature, with the largest temperature difference $T_{a,out} - T_{a,in} = 12$ K for $Q_{\text{solar}} = 28.3$ kW/m. The experimental values of the inner absorber surface temperature $T_{a,in}$ were derived from the temperatures measured at the center of the absorber $T_{a,center}$ using the radiosity method (see Appendix A). As expected, all temperatures increased with the power input. The maximum $T_{a,in}$

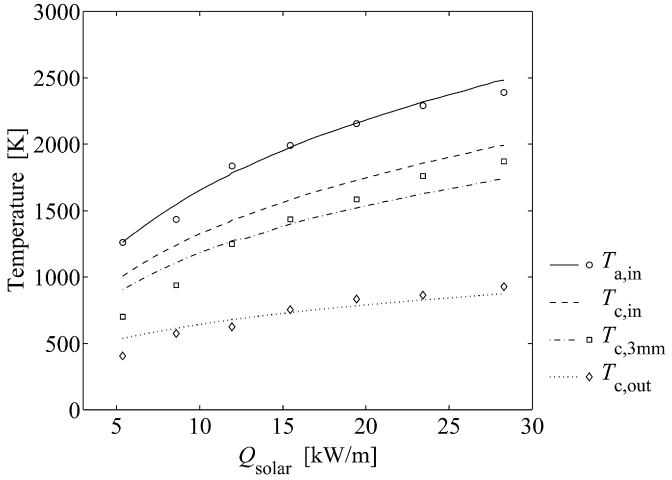

Fig. 4. Numerically calculated (curves) and experimentally measured (markers) temperatures at the inner absorber surface $T_{a,in}$, the inner cavity surface $T_{c,in}$, the outer cavity surface $T_{c,out}$, and 3 mm behind the inner cavity surface $T_{c,3\,mm}$, as a function of the incoming solar power per unit length Q_{solar}.

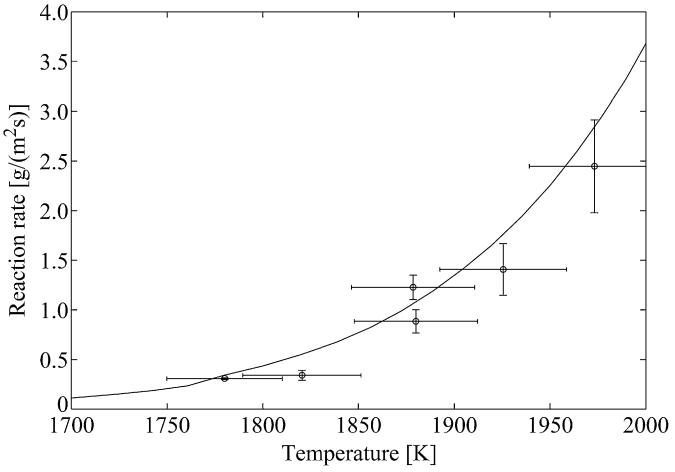

Fig. 5. Experimentally measured (markers) and theoretically calculated (curve) ZnO decomposition rates.

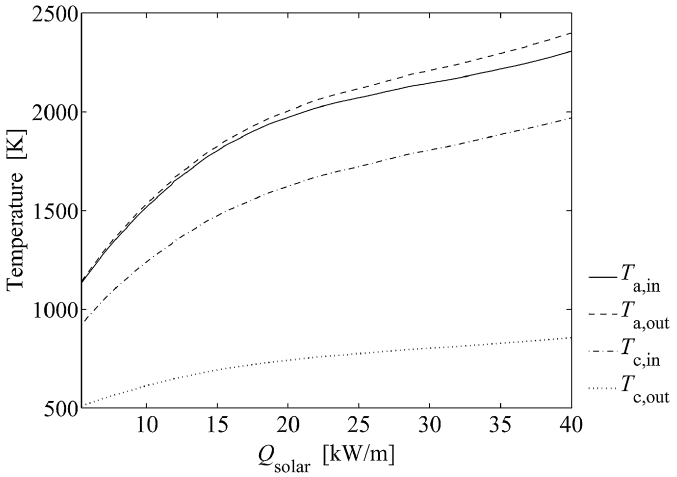

Fig. 6. Numerically calculated steady-state temperatures of the inner/outer absorber ($T_{a,in}$ and $T_{a,out}$) and inner/outer cavity surfaces ($T_{c,in}$ and $T_{c,out}$) as a function of the input solar power per unit length Q_{solar}.

was 2490 K, which exceeded Al_2O_3 m.p. (local melting was observed), while $T_{c,in}$ was about 500 K lower and $T_{c,out}$ never exceeded 1000 K. The maximum temperature difference between inner and outer cavity walls was 1120 K, which lead to the formation of local cracks in the YO_2-stabilized ZrO_2. The mean relative difference between measured and calculated values was 4.61% with a standard deviation ±4.87%, due mainly to discrepancies between real material properties and those extracted from literature for the model.

In batch-mode experiments, pre-sintered ZnO plates with an average surface area per unit length of $A_{ZnO} = 0.0446$ m^2/m were placed inside the absorber tube. The products Zn(g) and O_2 were carried by an Ar flow of 1 l_n/min to a quench unit incorporated at the reactor exit. Quenching is accomplished by contact to cold surfaces and by dilution through an annular channel made of two concentric tubes, with the outer one being water-cooled and the inner one having a porous wall for the injection of an inert gas. During a typical experimental run, the absorber was heated to the desired temperature, maintained isothermally for 10 min, and cooled to ambient temperature. The heating rate was relatively slow, about 40 K/min, since preliminary runs have shown that ceramic casting components, such the Al_2O_3 tube, poorly withstand severe thermal shocks. This is in contrast to direct-absorption reactor concepts, where the reactants are directly exposed to high-flux solar irradiation and can be heated at rates exceeding 1000 K/s [7]. The average reaction rate was determined using the weight loss by the ZnO plate. No reaction was observed at below 1750 K. The reaction rates obtained from six experimental runs carried out in the range 1780–1975 K are shown in Fig. 5, along with the theoretically calculated rates (curve) using the kinetic rate law of Eq. (17). Error bars result from the inaccuracies in the measurement devices (balance ±0.0015 g, dimensions ±0.05 mm, temperature ±2% of the reading). An 8-fold increase in the reaction rate was obtained in the range considered, with a peak rate of 2.446 g m^{-2} s^{-1} at 1975 K. Note that in these experimental runs, Zn(g) and O_2 exiting the reactor underwent recombination in the quench unit, as indicated by gas chromatography of the gaseous products and X-ray diffraction of the solid products.

5. Numerical simulation of the continuous chemical process

Numerical simulations of the reactor were performed assuming continuous feeding of reactants ($\dot{n}_{0,ZnO} = 3.07 \times 10^{-3}$ mol/s) and removal of products. Calculated temperature variations as a function of Q_{solar} in the range 5.4–40.0 kW/m (equivalent to a mean radiative flux at the CPC exit in the range 382–2830 kW/m^2) are plotted in Fig. 6 for steady-state conditions. Overall, temperatures are lower than those obtained without chemistry (Fig. 4) due to the additional heat sink resulting from heating the reactants ($Q_{reactants}$) and from the endothermic chemical reaction ($Q_{chemistry}$), as observed especially at above 1800 K for higher reaction extents X_{ZnO} (see also Fig. 7). For $Q_{solar} = 28.3$ kW/m, $T_{a,in}$ reaches 2120 K, about 370 K lower than in the case without chemistry. For

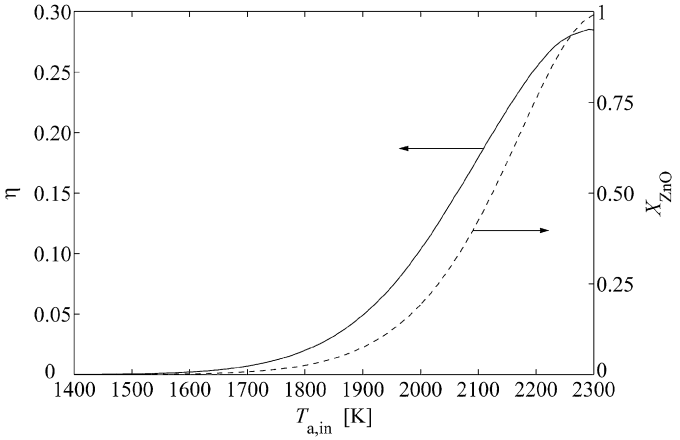

Fig. 7. Solar-to-chemical energy conversion efficiency and chemical reaction extent as a function of the inner absorber surface temperature.

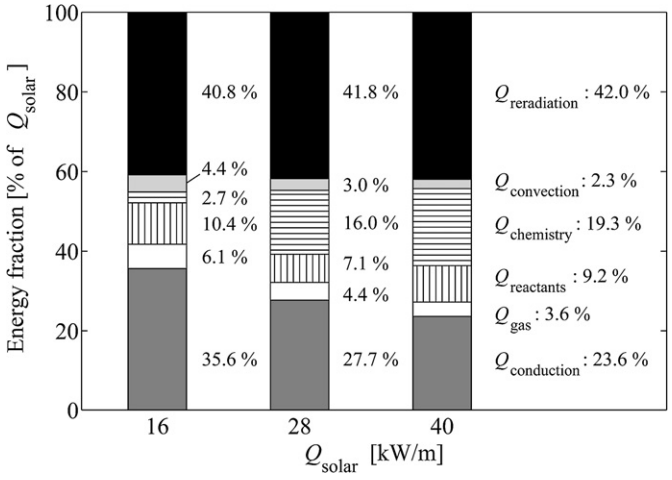

Fig. 8. Energy balance at input solar power levels of 16, 28 and 40 kW/m (per unit length of absorber), obtained by continuous-mode thermochemical process simulation.

$Q_{\text{solar}} = 40.0$ kW/m, $T_{\text{a,out}} = 2400$ K, $T_{\text{a,in}} = 2300$ K, $T_{\text{c,in}} = 1970$ K, and $T_{\text{c,out}} = 860$ K, and near reaction completion is attained (see also Fig. 7).

The solar-to-chemical energy conversion efficiency η is defined as the portion of the input solar power absorbed by the chemical reactants, both in the form of sensible heat and chemical process heat,

$$\eta = \frac{X_{\text{ZnO}} \cdot Q_{\text{reactants}} + Q_{\text{chemistry}}}{Q_{\text{solar}}} \tag{19}$$

Fig. 7 shows η and X_{ZnO} as a function of the inner absorber surface temperature, assuming no recombination of the products exiting the solar reactor. At $T_{\text{a,in}} = 2300$ K, X_{ZnO} approaches nearly completion, resulting in a maximum η of 28.5%. This predicted maximum efficiency is significantly higher than the one reported for the direct-absorption reactor operated at 2000 K and a solar power input of 9.1 kW, yielding a decomposition rate of 12 g/min, but an increase of the temperature to 2300 K could significantly augment the kinetics and, consequently, boost its efficiency [10]. Finally, Fig. 8 shows the overall energy balance calculated for $Q_{\text{solar}} = 16, 28$, and 40 kW/m. The power per unit length is indicated in percent of the solar power input. Re-radiation and conduction losses are predominant, with the latter decreasing from 36 to 24% over the power range considered. For $Q_{\text{solar}} = 16$ kW/m, $Q_{\text{chemistry}} = 0.027 Q_{\text{solar}}$ because of the relatively low reactor temperatures and, consequently, poor chemical conversion. Obviously, increasing Q_{solar} leads to higher temperatures, faster kinetics, and thereby higher chemical conversions, but at the expense of higher re-radiation losses. The energy fraction consumed by chemistry peaks at 22.5% for $Q_{\text{solar}} = 36.8$ kW/m (not shown in the graph), corresponding to a reactor temperature of 2245 K (ZnO melting point). Further temperature increase implies a decrease of the reaction enthalpy from 450 to 380 kJ/mol. For $Q_{\text{solar}} = 40$ kW/m, the reactor temperature reaches 2300 K and $\eta = 28.5\%$. $Q_{\text{chemistry}}$ and $Q_{\text{reactants}}$ represent 19 and 9% of Q_{solar}, respectively.

6. Summary and conclusions

We designed, fabricated, and tested a cylindrical cavity-receiver containing a tubular absorber for effecting high-temperature thermochemical reactions using concentrated solar energy. The reactor was modeled using a 2D steady-state formulation coupling radiation, conduction, and convection heat transfer to the chemical kinetics, and solved using Monte Carlo and finite difference techniques. The numerically computed temperatures and reaction rates were in reasonable good agreement with the experimentally measured values obtained from tests performed in a high-flux solar simulator. Major heat losses were re-radiation through the aperture and conduction through the reactor walls. Simulation of a continuous flow process predicts nearly completion of the reaction extent and maximum solar-to-chemical energy conversion efficiency of 28.5% at a reactor temperature of 2300 K for an input solar power per unit length of absorber of 40 kW/m. The technical feasibility and efficient performance of the continuous-mode thermochemical process using the proposed cavity-receiver/tubular-absorber reactor concept remain to be experimentally demonstrated.

Acknowledgements

Funding by the ETH Research Grant TH-39/04-3 and the BFE-Swiss Federal Office of Energy is gratefully acknowledged. We thank P. Coray for the heat flux measurements at the ETH's high-flux solar simulator.

Appendix A

The temperature of the inner absorber surface is derived from the temperature measured at the center of the absorber by a shielded thermocouple. Application of the radiosity method to the enclosure of Fig. 9 yields a system of equations in terms of the net radiative heat fluxes and temperatures [31]:

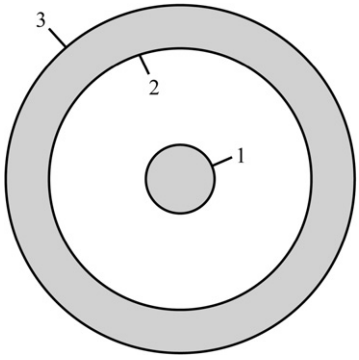

Fig. 9. Scheme of thermocouple (1: shield surface) placed concentric with the absorber (2: inner surface, 3: outer surface).

$$\sum_{j=1}^{N}\left(\frac{\delta_{ij}}{\varepsilon_j} - F_{i-j}\frac{1-\varepsilon_j}{\varepsilon_j}\right)q_j = \sum_{j=1}^{N}(\delta_{ij} - F_{i-j})\sigma T_j^4$$

for $i = 1..3$

where $i = 1, 2$, and 3 refer to the shield, inner absorber, and outer absorber surfaces, respectively. The corresponding view factors are $F_{1-1} = 0$, $F_{1-2} = 1$, $F_{2-1} = r_1/r_2$, and $F_{2-2} = 1 - r_1/r_2$. Solving the system of equations yields, $Q_1 = 2\pi r_1\sigma(T_1^4 - T_2^4)/\psi$, with $\psi = \frac{1}{\varepsilon_1} + \frac{r_1}{r_2}(\frac{1}{\varepsilon_2} - 1)$. Since $Q_1 = -Q_2 = 2\pi k(T_2 - T_3)/\ln(r_3/r_2)$, the implicit equation for T_2 is

$$T_2 = \left[T_1^4 + k\psi(T_3 - T_2)/r_1\sigma\ln(r_3/r_2)\right]^{1/4},$$

which is solved iteratively.

References

[1] A. Steinfeld, Solar thermochemical production of hydrogen—a review, Solar Energy 78 (2005) 603–615.

[2] A. Steinfeld, M. Schubnell, Optimum aperture size and operating temperature of a solar cavity-receiver, Solar Energy 50 (1993) 19–25.

[3] W.T. Welford, R. Winston, High Collection Nonimaging Optics, Academic Press, San Diego, 1989.

[4] C. Perkins, A.W. Weimer, Likely near-term solar-thermal water splitting technologies, Int. J. Hydrogen Energy 29 (2004) 1587–1599.

[5] R. Palumbo, J. Lédé, O. Boutin, E. Elorza Ricart, A. Steinfeld, S. Möller, A. Weidenkaff, E.A. Fletcher, J. Bielicki, The production of Zn from ZnO in a high-temperature solar decomposition quench process—I. The scientific framework for the process, Chem. Eng. Sci. 53 (1998) 2503–2517.

[6] A. Steinfeld, Solar hydrogen production via a two-step water-splitting thermochemical cycle based on Zn/ZnO redox reactions, Int. J. Hydrogen Energy 27 (2002) 611–619.

[7] P. Haueter, S. Möller, R. Palumbo, A. Steinfeld, The production of zinc by thermal dissociation of zinc oxide—solar chemical reactor design, Solar Energy 67 (1999) 161–167.

[8] S. Möller, R. Palumbo, The development of a solar chemical reactor for the direct thermal dissociation of zinc oxide, J. Solar Energy Eng. 123 (2001) 83–90.

[9] R. Müller, P. Haeberling, R.D. Palumbo, Further advances toward the development of a direct heating solar thermal chemical reactor for the thermal dissociation of ZnO(s), Solar Energy 80 (2006) 500–511.

[10] R. Müller, W. Lipiński, A. Steinfeld, Transient heat transfer in a directly-irradiated solar chemical reactor for the thermal dissociation of ZnO, Appl. Therm. Eng., in press.

[11] C. Wieckert, A. Meier, A. Steinfeld, Indirectly irradiated solar receiver-reactors for high-temperature thermochemical processes, J. Solar Energy Eng. 125 (2003) 120–123.

[12] T. Melchior, A. Steinfeld, Radiative transfer within a cylindrical cavity with diffusely/specularly reflecting inner walls containing an array of tubular absorbers, J. Solar Energy Eng., in press.

[13] D. Hirsch, P.v. Zedtwitz, T. Osinga, J. Kinamore, A. Steinfeld, A new 75 kW high-flux solar simulator for high-temperature thermal and thermochemical research, J. Solar Energy Eng. 125 (2003) 117–120.

[14] J.T. Farmer, J.R. Howell, Comparison of Monte Carlo strategies for radiative transfer in participating media, in: T.F. Irvine, J.P. Hartnett (Eds.), Advances in Heat Transfer, vol. 31, Academic Press, ISBN 0-12-020031-7, 1998, pp. 333–429.

[15] Y.S. Touloukian, D.P. De Witt, Thermophysical Properties of Matter, Thermal Radiative Properties: Nonmetallic Solids, vol. 8, IFI/Plenum, New York, Washington, 1972.

[16] Y.S. Touloukian, R.W. Powell, C.Y. Ho, P.G. Klemens, Thermophysical Properties of Matter, Thermal Conductivity: Nonmetallic Solids, vol. 2, IFI/Plenum, New York, Washington, 1970.

[17] Zircar Zirconia, Inc., Product Data Bulletin #A-D, www.zircarzirconia.com/doc/A-D_FBD.pdf, 2006.

[18] T.H. Kuehn, R.J. Goldstein, Correlating equations for natural convection heat transfer between horizontal circular cylinders, Int. J. Heat Mass Transfer 19 (1976) 1127–1134.

[19] M.J. Shilston, S.D. Probert, Thermal insulation provided by plain, horizontal annular cavities containing atmospheric pressure air, Applied Energy 5 (1979) 61–80.

[20] R.F. Babus'Haq, S.D. Probert, M.J. Shilston, Natural convection across cavities: design advice, Applied Energy 20 (1985) 161–188.

[21] R.F. Babus'Haq, S.D. Probert, Finite-element analyses of natural convections across horizontal air-filled cavities each surrounding a heated pipe, Applied Energy 30 (1988) 15–28.

[22] F.P. Incropera, D.P. DeWitt, Fundamentals of Heat and Mass Transfer, fifth ed., John Wiley & Sons, 2002.

[23] A.M. Clausing, J.M. Waldvogel, L.D. Lister, Natural convection from isothermal cubical cavities with a variety of side facing apertures, J. Heat Transfer 109 (1987) 407–412.

[24] W.B. Stine, C.G. McDonald, Cavity receiver heat loss measurements, in: Proc. of ISES World Congress, Kobe, Japan, 1989.

[25] U. Leibfried, J. Ortjohann, Convective heat loss from upward and downward-facing cavity solar receivers: measurements and calculations, J. Sol. Energy Eng. 117 (1995) 75–84.

[26] T. Taumoefolau, S. Paitoonsurikarn, G. Hughes, K. Lovegrove, Experimental investigation of natural convection heat loss from a model solar concentrator cavity receiver, J. Sol. Energy Eng. 126 (2004) 801–807.

[27] N. Sendhil Kumar, K.S. Reddy, Numerical investigation of natural convection heat loss in modified cavity receiver for fuzzy focal solar dish concentrator, Solar Energy 81 (2007) 846–855.

[28] ANSYS CFX 10.0, 2005 (ANSYS, Inc.).

[29] S.H.P. Chen, S.C. Saxena, Thermal conductivity of argon in the temperature range 350 to 2500 K, Molecular Physics 29 (1975) 455–466.

[30] S. Möller, R. Palumbo, Solar thermal decomposition kinetics of ZnO in the temperature range 1950–2400 K, Chem. Eng. Sci. 56 (2001) 4505–4515.

[31] R. Siegel, J.R. Howell, Thermal Radiation Heat Transfer, fourth ed., Taylor & Francis, New York–London, 2002.